Surface & Coatings Technology 205 (2011) 5021–5027

Contents lists available at ScienceDirect

Surface & Coatings Technology

journal homepage: www.elsevier.com/locate/surfcoat

Impact phenomena in cold-spraying of titanium onto various ferrous alloys

T. Hussain [a,*], D.G. McCartney [b], P.H. Shipway [b]

[a] Centre for Energy and Resource Technology (CERT), School of Applied Sciences, Cranfield University, Bedford, MK43 0AL, UK
[b] Division of Materials, Mechanics and Structures, Faculty of Engineering, University of Nottingham, Nottingham NG7 2RD, UK

ARTICLE INFO

Article history:
Received 3 February 2011
Accepted in revised form 5 May 2011
Available online 12 May 2011

Keywords:
Cold spray
Impact
Titanium
Stainless steel
Armco iron
Carbon steel

ABSTRACT

The impact and deformation behaviour of particle and substrate in cold-spraying is dictated by the high strain rate materials behaviour which affects bonding. In this study, titanium particles have been deposited onto three different ferrous alloy substrates, namely low carbon steel, an Armco iron, and an austenitic stainless steel. The deformation behaviour of the particle–substrates was characterised by scanning electron microscopy and modelled using Johnson–Cook material parameters at high strain rate. Localised deformation of the Armco iron was observed following deposition of titanium particles, whereas a combination of particle–substrate deformation was observed in titanium-low carbon steel and titanium-austenitic stainless steel. The chemical composition i.e., carbon content of the substrate alters the high strain rate deformation behaviour upon cold spraying. Jetting of titanium particles was observed following deposition onto low carbon steel and austenitic stainless steel while restricted jetting of titanium particles following deposition onto Armco iron was observed as the particles were embedded into the Armco iron.

1. Introduction

Cold gas dynamic spraying is a high strain-rate material deposition technique, in which powder particles (typically 10–40 μm in size) are accelerated to velocities of between 300 and 1200 m/s, and upon impact with a substrate (or previously deposited particles), deform plastically and adhere [1–3]. The cold-spraying of titanium and its alloys has received much attention in the literature, driven primarily by the possibility of surface engineering of components with a material with such desirable corrosion resistance and the potential for near-net-shape manufacturing [4–10]. Specifically, a barrier layer of titanium coating deposited onto a low carbon steel substrate has been shown to have the potential to prevent corrosion attacks in sea water [7,11] and titanium clad stainless steel is a desirable component for various applications in nuclear industry [12,13]. The impact and deformation behaviour in bonding of any deposited titanium layers onto a substrate are critical to the effectiveness of the layer in fulfilling its requirements.

There are several theories on the particle bonding in cold-spraying. The most popular theory is that when a particle impacts with a surface, one or both of the materials undergo high strain rate plastic deformation; when thermal softening dominates over work hardening, a sudden increase in temperature and strain rate occurs which results in a reduction of flow stress and a material jet is formed, composed of impacting material and substrate [1,3]. For metal-to-metal bonding to occur in cold-spraying, the impacting particle has to disrupt the surface oxide layer surrounding the particle and on the substrate surface [14]. It has been established that for a particle to adhere to a substrate, the particle has to impact at a velocity exceeding a so called *critical velocity* [1,3,15,16]. The critical velocity of a particle depends on a number of factors including particle–substrate materials, density, thermal conductivity, temperature, heat capacity, melting temperature, particle oxidation conditions etc. [17–19].

A number of numerical analyses have been published in the past decade which have attempted to understand deformation phenomena occurring in cold-spraying with the authors discussing how different spraying parameters influence this behaviour. The role of different substrates on cold spraying of copper, nickel and aluminium has been studied by several researchers [20–23]. A number of recent publications on cold-sprayed titanium coatings have addressed the effect of spraying process parameters, mechanical and microstructural properties, however, a systematic investigation of the role of various ferrous substrates on deposition of titanium has not yet been studied [8–10,24–33]. In the current study, the impact and bonding behaviour of such titanium particles onto three different iron based substrates were examined. Low-carbon steel (containing a small amount of carbon which alters its strain hardening properties) and Armco (American Rolling Mill Company) iron (a commercially-pure grade of iron with very low carbon content) were selected to investigate the role of carbon during the deformation between a ferrous alloy and an impacting titanium particle. In addition, it is known that austenitic stainless steel has very different material properties from that observed on Armco iron and low carbon steel, and as such, a 304 stainless steel was also employed as a substrate.

* Corresponding author. Tel.: +44 1234750111 E2822.
E-mail address: t.hussain@cranfield.ac.uk (T. Hussain).

0257-8972/$ – see front matter © 2011 Elsevier B.V. All rights reserved.
doi:10.1016/j.surfcoat.2011.05.003

2. Experimental

2.1. Materials

Commercial purity gas atomized titanium powder of size <25 μm (Pyrogenesis, Canada) was used as the cold-spray particle feedstock. Titanium powder was deposited onto three different substrates: Armco iron, low carbon steel, and austenitic stainless steel (304). The chemical compositions of the substrates were measured using optical emission spectroscopy (Foundry-Master UV, Oxford Instruments, Bucks, UK) and are shown in Table 1.

2.2. Cold-spraying

Cold-spraying of titanium powder was performed with an in-house built cold gas spraying system at the University of Nottingham described elsewhere [21,34]. The convergent-divergent nozzle had a throat diameter of 1.35 mm, with an area expansion ratio of ~8.8 and the divergent section with a length of 100 mm. The system utilized room temperature helium at 2.9 MPa for the primary accelerating gas and nitrogen as the powder carrier gas. The pressure of the carrier gas was set approximately 0.1 MPa higher (~ 3.0 MPa) than the primary gas pressure to ensure powder feeding into the primary gas flow. A high pressure powder feeder (Praxair 1264HP, Indianapolis, IN, USA) was used during the cold-spraying process, with a 120 hole feeding wheel. The nozzle-substrate standoff distance for all the spray runs was fixed at 20 mm. All substrates were sequentially ground with different grade SiC papers to a 1200 grit finish and polished with 6 and 1 μm diamond paste. The polished samples were rinsed with methyl alcohol and dried using compressed air immediately prior to spraying. Substrates were then clamped side-by-side on an X–Y traverse table which controlled the relative motion between the nozzle and the sample. The table moved the samples relative to the nozzle. The lowest powder feed rate (with a feeding wheel speed of 0.5 rpm giving a feed rate of ~5 g/min) and the highest scan rate (traverse speed of 500 mm/s) were used to achieve the lowest impacting particle flux onto the substrate achievable by this system. Single pass of the gun was used on each of the substrates to produce the samples.

2.3. Sample characterization

Sample cross-sections were prepared by sectioning with a diamond slitting wheel; sections were sequentially ground using SiC paper to P1200 grit and polished with 0.1 μm colloidal silica final polishing solution on soft cloth wheels. A FEI XL30 (FEI Europe, Eindhoven, The Netherlands) scanning electron microscope (SEM) operating at 20 kV was used to examine the microstructure using secondary electron (SE). Image analysis software ImageJ (U.S. National Institute of Health, MD) was used on SEM images to quantify area fractions of particles deposited onto substrates in swipe tests. For each condition, five representative images were selected for measurement.

The particle size analysis was measured by laser diffractometry (Laser Mastersizer, Malvern Instruments, Malvern, UK). To examine the microstructure, all the substrates were etched lightly and examined by optical microscopy. Low carbon steel and Armco iron were etched using 5% nital and austenitic stainless steel was etched using aqua regia solution.

Micro-hardness indentations were made on finely-polished cross-sections of the substrates using a Leco M400 micro-hardness tester (Cheshire, UK). The values of Vickers micro-hardness of the substrates quoted are the average of five measurements made using a 100 gf load for a loading time of 15 s. To measure the micro-hardness of the feedstock particles, the powders were mounted in resin, ground using P1200 grit, polished with 6 and 1 μm diamond grit on soft cloth wheels. Due to the small size of the particles, a load of 10 gf was used for a loading time of 15 s to measure the micro-hardness. Ten measurements were taken at the centre of the cross-section of the particles and the average value is reported with the standard error of the mean.

3. Results

3.1. Characterization of feedstock powder

Fig. 1(a) shows the morphology of the feedstock gas atomized powder (supplier specified size range of <25 μm). It can be seen that the particles have a spherical morphology with very few satellite particles. Particle size analysis shows approximately 10 vol.% of particles are above 25 μm in Fig. 1(b) and the mean size of the particles is 18 μm.

3.2. Characterization of substrates

The etched microstructures of all three substrates are shown in Fig. 2. Low carbon steel contains 0.04% carbon and composed of α-Fe and pearlite. Fig. 2(a) shows equiaxed grains of α-Fe with an average grain size of ~10 μm and pearlite (the darker contrast in the optical microscopy image). Armco iron is an ultra low carbon commercially pure ingot iron which has a body centred cubic (bcc) structure similar to low carbon steel. Fig. 2(b) shows that the microstructure of Armco iron is composed of α-Fe with grains in the order of hundreds of microns in size. The austenitic stainless steel has a γ-Fe face centred cubic (fcc) structure. Fig. 2(c) shows etched microstructure of austenitic stainless steel with uniform grain sizes of ~50 μm and a few twin grain boundaries.

The micro-hardness of the three iron based alloys are shown in Table 2. The austenitic stainless steel is the hardest of all the materials with a hardness of 222 ± 2 kgf/mm^2 and Armco iron is the softest with a hardness of 123 ± 1 kgf/mm^2. Low carbon steel has a hardness of 167 ± 1 kgf/mm^2, which is higher than Armco iron due to presence of higher amount of carbon. The feedstock power particles exhibited a micro-hardness of 183 ± 13 kgf/mm^2 which is in reasonable agreement with values reported by other researchers for spherical titanium powders [31,35–37].

3.3. Deposition of titanium powder onto ferrous alloys

Cold-sprayed spherical titanium particles following deposition onto low carbon steel, Armco iron, and austenitic stainless steel substrates are shown in Fig. 3. The substrate surface of low carbon steel (Fig. 3a1) shows a large number of craters following cold-spraying. In cold-spraying, the craters are formed on the substrate when the impacting particles do not bond with the substrate [2,3,38]. In addition, weakly bonded particles

Table 1
Chemical compositions of the low carbon steel, Armco iron, and stainless steel (304) measured using optical emission spectroscopy.

Substrate types	Element (wt.%)										
	C	Cr	Ni	Mo	P	S	Mn	Si	Al	V	Fe
Low carbon steel	0.04	0.03	0.01	–	0.01	0.02	0.17	–	0.03	–	Bal.
Armco iron	<0.005	0.01	0.02	–	–	0.01	0.04	–	0.01	–	Bal.
Stainless steel, 304	0.05	17.8	8.31	0.18	0.04	–	1.24	0.34	–	0.08	Bal.

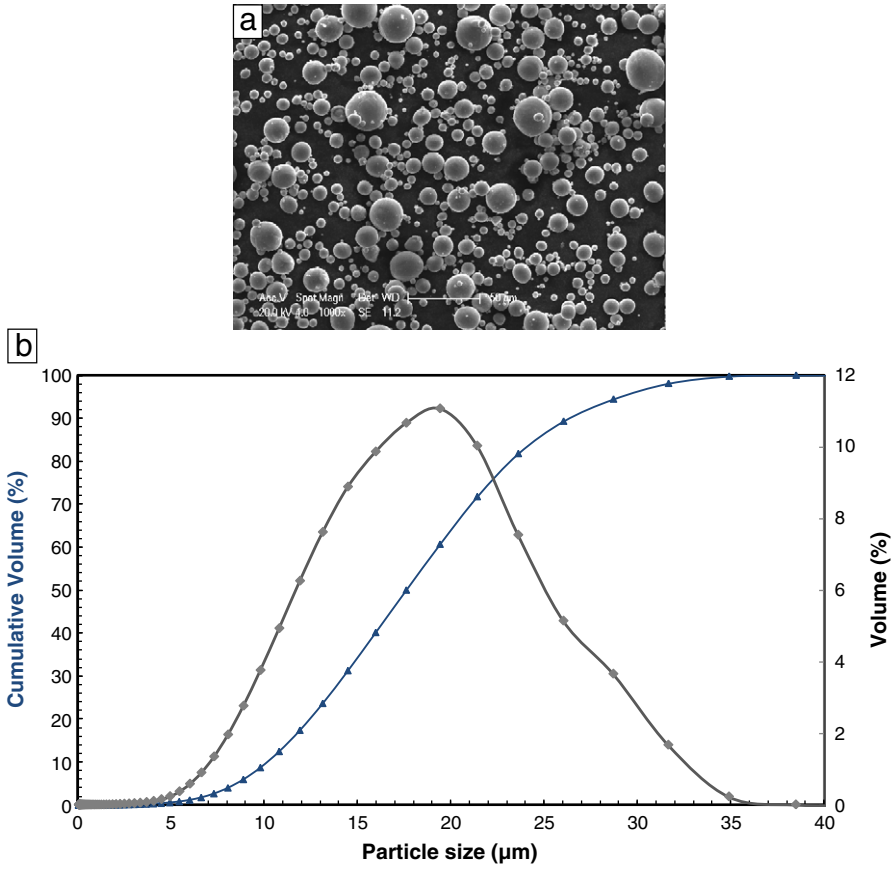

Fig. 1. (a) Secondary electron (SE) image of spherical titanium powder (b) powder particle size distribution.

could have been removed by high gas jet pressure [35]. Fig. 3(b1, c1) shows a much wider size range of particles which have deposited onto the Armco iron and stainless steel substrates. Moreover, in Fig. 3(b1, c1), a significant reduction in the incidence of crater formation is observed compared to low carbon steel substrate. In comparing between the three material types, there are no changes in the nature of the spray plume characteristics (as there would be if the powder type or spraying conditions were changed); as such, all three materials were exposed to the same particle flux but image analysis of Fig. 3(a1, b1, c1) indicates that the area fraction of titanium bonded to the substrate surface is ~0.25, 0.50 and 0.40 (all ± 0.05) for the low carbon steel, Armco iron and austenitic stainless steel substrates respectively.

Tilted view images of titanium particles onto low carbon steel, Armco iron, and austenitic stainless steel are shown in Fig. 3(a2, b2, c2). Titanium particles deposited onto low carbon steel substrate show formation of metallic jet, marked by an arrow in Fig. 3(a2). Fig. 3(a3) shows the cross-section of a titanium particle deposited onto low carbon steel and the particle shows formation of a metal-jet on both sides. In contrast, a different mode of particle-substrate interaction is observed following cold-spay impact of a titanium particle onto an Armco iron substrate (Fig. 3b2), where little particle flattening was observed. The cross-section of a deposited particle onto Armco iron in Fig. 3(b3) shows that the particle is embedded into the Armco iron substrate which deformed significantly following deposition; in contrast to the behaviour observed for low carbon steel substrates, no material jetting upon impact is observed in this case. Fig. 3(c2) shows a titanium particle deposited onto austenitic stainless steel and the jet from the particle is clearly seen. Fig. 3(c3) shows the cross-section of a titanium particle onto austenitic stainless steel substrate and the material jet is marked with an arrow.

All the titanium particles deposited onto each substrate can be classified into three different groups: particles showing “no jetting”, “little jetting” and “extensive jetting”. In each particle–substrate combination, twenty cross-section images of the particles from the centre of the deposited track were studied. In the case of titanium deposited onto low carbon steel, the fraction of the particles showing “little jetting” was 0.4 and the fraction of the particles showing “extensive jetting” was 0.6. However, in titanium deposited onto Armco iron case, 0.85 fraction of the particles showed “no jetting” but showed significant substrate deformation, ~0.07 fraction showed “little jetting” and ~0.07 fraction showed “extensive jetting”. In addition, 0.2 fraction of the titanium particles deposited onto the stainless steel substrate showed “little jetting” and 0.8 fraction of the particles showed “extensive jetting”. In summary, majority of the particles deposited onto Armco iron did not result in jetting but showed significant substrate deformation, whereas particles deposited onto low carbon steel and stainless steel substrates resulted in “extensive jetting”. It should also be noted that a significant fraction of titanium particles deposited onto low carbon steel (0.4) resulted in “little jetting”.

4. Discussion

4.1. Impact phenomena in cold-spraying of titanium onto ferrous alloys

4.1.1. Particle substrate deformation behaviour

Particle bonding in cold-spraying is dependent on plastic deformation of the impacting particles and the substrates. Adiabatic shear instability occurs at the particle–substrate interface, which results in abnormal temperature and strain histories and thus to the collapse of stresses; visco-plastic behaviour of the metals is generally postulated due to dominance of thermal softening over work hardening [1,20]. When a harder material impacts with a softer material, the plastic energy is primarily dissipated in the softer counterpart [20]. As such, when titanium impacts with the softer Armco iron, the plastic deformation is

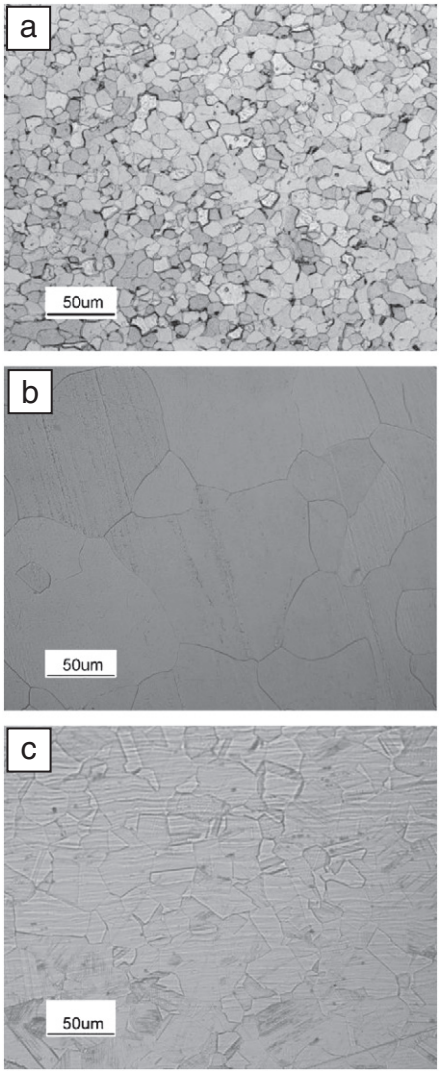

Fig. 2. Optical microscope images of etched microstructure of (a) low carbon steel, (b) Armco iron, and (c) austenitic stainless steel.

mostly in the Armco iron. The deformation of Armco iron is far greater than the deformation of low carbon steel following impact by titanium particles, an observation which may be explained as follows. Armco iron contains less than <0.005 wt.% carbon and 0.04 wt.% manganese; in contrast, the low carbon steel contains 0.04 wt.% carbon and 0.17 wt.% manganese (Table 1), resulting in a higher hardness for the carbon steel compared to the Armco iron. The amount of carbon and manganese present in the carbon steel changes the high strain rate behaviour [39] and therefore will affect the way in which particle and substrate deform upon impact. Although very low strain rate hardness measurements cannot predict the high strain rate deformation behaviour associated with impact, the softest material (Armco iron) is also observed to be the material which deformed most significantly during particle impact.

Table 2
Micro-hardness values of the low carbon steel, Armco iron, and stainless steel (304) substrates. The micro-hardness value of titanium powder used in this study was 183 ± 13 kgf/mm^2.

Substrate	Micro-hardness (kgf/mm^2)
Low carbon steel	167 ± 1
Armco iron	123 ± 1
Stainless steel, 304	222 ± 2

Cold-spraying of titanium onto low carbon steel resulted in a small fraction of deposition (0.25 ± 0.05) and a large number of craters on the surface. In addition, in the case of low carbon steel the particles of smaller diameter have been rebounded while the particles of large diameter have been deposited (Fig. 3 a1, b1, c1). It is not clear at this stage why the fraction of deposited particle on low carbon steel is the lowest of all three substrates, but one could speculate that the bonding of titanium with low carbon steel is weaker and hence the loosely bonded particles with smaller diameter were removed by the impingement of the high pressure jet (2.9 MPa in this case) [35]. It has also been reported that successful build-up of titanium coatings onto low carbon steels was proven to be challenging [40]. Moreover, the hardness of the titanium particle feedstock is 183 ± 13 kgf/mm^2 which is higher than that of Armco iron (123 ± 1 kgf/mm^2) but not significantly different from the hardness of the low carbon steel (167 ± 1 kgf/mm^2), taking the standard error of the mean into consideration. Previous numerical simulations [20] showed that critical velocities of particles with same hardness with the substrate (i.e. titanium on low carbon steel) are higher than those of particles with hardness higher than the hardness of the substrate (i.e. Ti on Armco iron). The fraction of particles deposited onto the Armco iron is high (0.5 ± 0.05), however the large fraction of the deposited particles do not show any evidence of jetting. Despite this lack of jetting the particles are deposited due to the localised deformation of the substrate which can act as an "anchoring mechanism". On the other hand, a large fraction of deposited titanium particles on the austenitic stainless steel resulted in "extensive jetting". This extensive jetting of the particles contributed to bonding to the stainless steel substrate. It is possible that the higher hardness of the stainless steel substrate played a role in this extensive jetting of titanium.

4.1.2. Johnson–Cook plasticity model of material behaviour

The impact behaviour of particles at high strain rate can be described by the Johnson–Cook model. The Johnson–Cook plasticity model [41], which includes strain hardening, strain-rate hardening and thermal softening effects, can be described by the following equation:

$$\sigma = \left[A + B\varepsilon_p^n\right]\left[1 + C\, ln\left(\frac{\dot{\varepsilon}_p}{\dot{\varepsilon}_0}\right)\right]\left[1-\left(T^*\right)^m\right] \quad (1)$$

where σ is the equivalent flow stress, ε_p is the equivalent plastic strain, $\dot{\varepsilon}_p$ is the equivalent plastic strain rate, $\dot{\varepsilon}_0$ is the reference strain rate and T^* is the normalised temperature. A, B, C, m, and n are material specific properties; A is the yield stress in a simple quasi static tension/compression test, B is the stain-hardening parameter, C is the dimensionless strain-rate hardening coefficient and n, m are exponents of strain-hardening and thermal-softening terms. The normalised temperature T^* is described as follows

$$T^* = \begin{cases} 0; & T<T_{trans} \\ (T-T_{trans})\,/\,(T_{melt}-T_{trans}); & T_{trans} \le T \le T_{melt} \\ 1; & T_{melt}<T. \end{cases} \quad (2)$$

T_{melt} is the melting temperature above which the flow stress of the material is zero and T_{trans} is a reference temperature above which thermal softening is assumed to occur. The Johnson–Cook model parameters experimentally extracted at relatively low strain rates (typically 10^3–10^5/s) may not be adequate to describe the higher range of strain-rate estimated for cold-spray and warm-spray particle impact (typically 10^6–10^9/s [1,3,42]). Nevertheless, the Johnson–Cook model will provide with a way to compare the flow stresses of different materials at elevated strain-rates.

To calculate the stress strain behaviour of a material using the Johnson–Cook model requires estimates of the appropriate temperature and strain rate to be made. These estimates were made as follows.

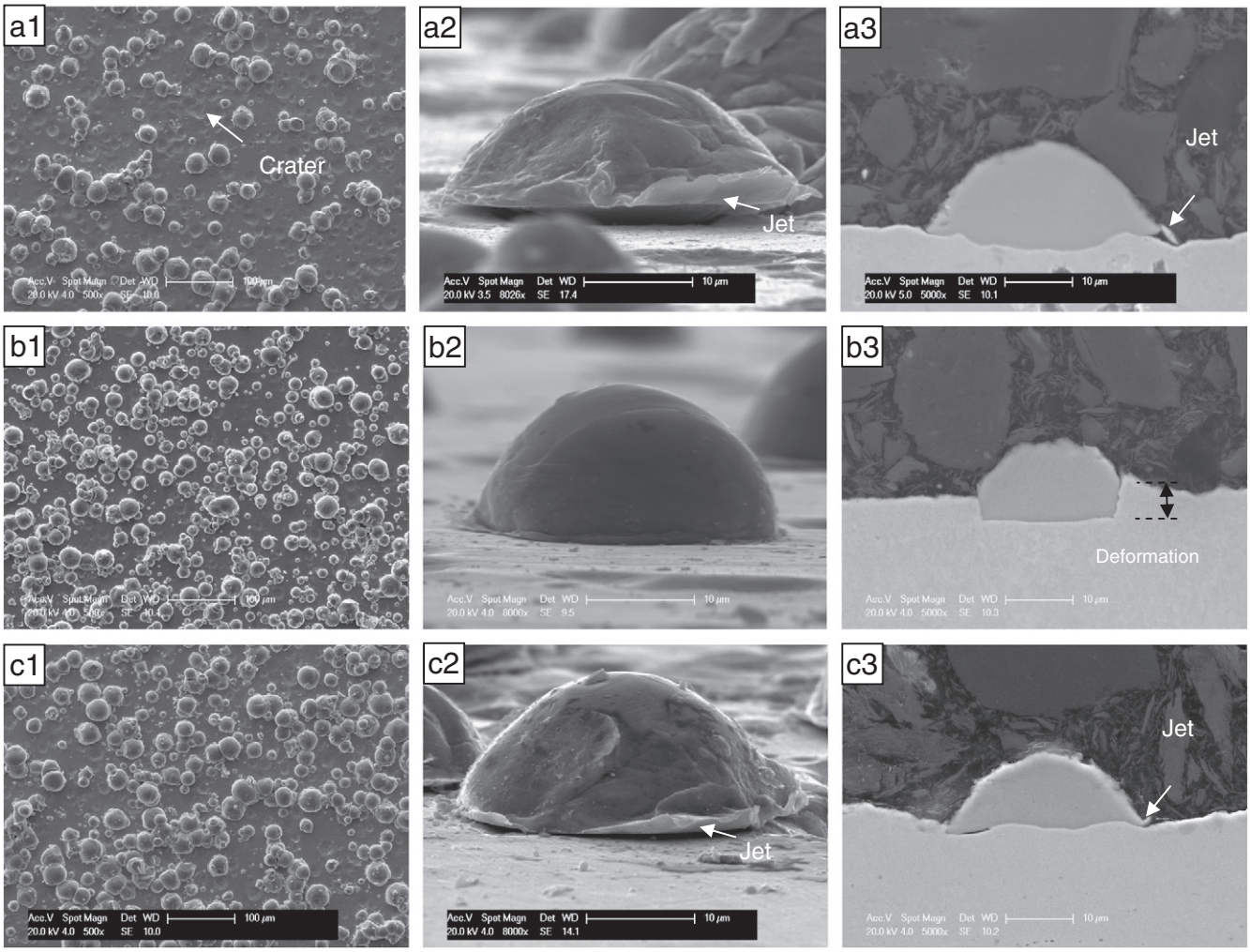

Fig. 3. Low-magnification SE images of rounded titanium particles sprayed using room temperature helium onto (a1) low carbon steel, (b1) Armco iron, (c1) austenitic stainless steel; 86° tilted view of as-sprayed titanium particles onto (a2) low carbon steel, (b2) Armco iron, (c2) austenitic stainless steel, and cross-section of as-sprayed titanium particles onto (a3) low carbon steel, (b3) Armco iron, (c3) austenitic stainless steel.

4.1.2.1. Estimate of strain rate.

The strain rate of a perfectly plastic impact of a spherical particle onto metal substrate is given by Hutchings [43]:

$$\dot{\varepsilon}_p \approx \frac{2^{3/2}}{5\pi}\frac{v^{1/2}}{r}\left(\frac{3P}{2\rho}\right)^{1/4} \quad (3)$$

where, P is the mean pressure acting on the sphere during indentation, ρ is the density, r is the radius of the sphere and v is the velocity of the sphere. In computing the strain rate, a mean pressure P = 1795 MPa was taken corresponding to quasistatic indentation hardness of the titanium powder (183 kgf/mm^2), ρ = 4500 kg/m^3 and v = 600 m/s and r = 10 μm. The calculated strain rate under these conditions is ~10^7/s.

4.1.2.2. Estimate of temperature.

According to slip-line field theory, when a rigid punch deforms an ideally plastic material, the zone of plastic deformation is approximately twice the diameter of the punch [44]. If we assume a 10 μm radius spherical titanium particle impacts the substrate, the radius of the plastic deformation zone on the substrate will be ~20 μm. The rigid punch assumptions will not be valid in cold-spraying due to plastic deformation of the particles upon impact; nevertheless this assumption will provide an approximate value to perform the necessary calculations. If the plastic zone on the substrate is assumed to be hemispherical in shape, then the volume of the plastic zone can be calculated using $V = 2/3\,\pi r'^3$, here $r' = 20$ μm, which gives 1.67×10^{-14} m^3. The kinetic energy of a particle can be calculated using, K.E = 1/2 mv^2. Using this equation, a 10 μm radius titanium particle travelling at 600 m/s has a kinetic energy of ~3.4×10^{-6} J. Assuming that this kinetic energy is dissipated over the entire plastic zone volume following impact (without any frictional loss) results in an energy density of 2×10^8 J/m^3. The temperature rise in the adiabatic shear bands (ASB) at high strain rates >10^3/s is considered adiabatic, and the plastic deformation energy is converted to heat and leads to a rise in temperature which is given by Yang et al. [45].

$$T - T_0 = \frac{\beta}{C_v\rho}\int_0^{\varepsilon} \sigma d\varepsilon \quad (4)$$

T is temperature at the adiabatic shear band, T_0 is initial temperature, C_v is heat capacity and β is a constant, which, for adiabatic processes, is taken as 0.9 (90% of the energy converted to heat). For titanium $C_v = 528$ J/kg/K, $T_0 = 293$ K and kinetic energy dissipated $= 2\times10^8$ J/m^3, then the temperature rise at the adiabatic shear band is ~100 K. This value represents the mean rise in temperature at the adiabatic shear band. Eq. (4) has been widely used to calculate the rise in temperature at the adiabatic shear bands in processes like explosive welding [45,46].

Table 3
Material parameters for titanium, carbon steel, Armco iron and stainless steel in the Johnson–Cook equation.

Johnson–Cook parameters	Material types (with references for data)			
	Titanium [17]	Carbon steel [17]	Armco iron [34]	Stainless steel, 304 [39]
A, MPa	806.57	532.0	175	110
B, MPa	481.61	229.0	380	1500
n	0.319	0.3024	0.32	0.36
C	0.0194	0.0274	0.06	0.014
m	0.655	1.0	0.55	1
T_{melt}, K	1923	1793	1811	1694
T_{trans}, K	298	283	298	298
Ref strain rate/s	1	1	1	10^3

Table 3 shows the Johnson–Cook parameters for titanium, carbon steel, Armco iron, and austenitic stainless steel collected from the literature. Fig. 4 illustrates the flow stress of these materials at strain rate of 10^7/s at 373 K. In comparison to titanium, carbon steel and Armco iron, the flow stress of the austenitic stainless steel rises sharply with increasing plastic strain. The strain hardening parameter (B) for austenitic stainless steel is very high compared to those of titanium, carbon steel and Armco iron (Table 3). Fig. 4 shows the stress–strain curve of titanium is above the stress–strain curve of carbon steel and Armco iron for all the values of plastic strains. The flow stress values of Armco iron are always lower than those of carbon steel for all values of plastic strains implying that the degree of deformation of Armco iron will be greater compared to carbon steel. The stress–stain curves (under these high strain rate, high temperature conditions) for the austenitic stainless steel and titanium cross each other at a plastic strain of around 0.55. As such, the relative deformation behaviour of the titanium and the austenitic stainless steel will vary as a function of plastic strain. At plastic strains of less than 0.55, the deformation will predominantly take place in the austenitic stainless steel and above that value, the deformation will predominantly take place in titanium. It should be noted that the flow stress–strain curves available in Fig. 4 are for a particular temperature and a strain rate, which can only be applied to understand the deformation behaviour in an impact if both the particle and substrate have the same temperature and strain rate.

The area under the flow stress and plastic strain curve represents the plastic energy density involved in the deformation. If there is no loss of energy during the high strain rate deformation process, then the 2×10^8 J/m^3 of kinetic energy per particle will result in an equivalent plastic strain of 0.23 in carbon steel, 0.34 in Armco iron and 0.25 in austenitic stainless steel. The area under the curves was calculated using trapezoidal rule. It should be noted that Armco iron is expected to exhibit a plastic strain of ~1.5 times than that of carbon steel.

5. Conclusions

The impact and deformation behaviour in cold-spraying of titanium onto three ferrous alloys have been investigated experimentally and the observations were rationalised using the Johnson–Cook high strain rate material model. It can be concluded from this study that cold-spraying of titanium onto an Armco iron substrate results in a localised deformation of the substrate. However, in cold-spraying of titanium onto a low carbon steel substrate, the degree of localised deformation of the substrate is significantly less. The reduced level of carbon in Armco iron influences the high strain rate material properties, and hence alters the particle–substrate deformation behaviour in cold-spraying. The phenomenon of particle jetting upon impact is not generally observed following deposition of titanium onto an Armco iron (i.e. relatively softer counterpart) due to the localised deformation of the substrate. In contrast, jetting of titanium particles was generally observed following deposition onto low carbon steel and austenitic stainless steel substrates, which suggests that relatively harder ferrous alloys might promote particle jetting upon impact.

Acknowledgement

T. Hussain acknowledges financial support from the University of Nottingham through the award of Overseas Research Studentship (ORS) and an industrial sponsorship from TWI Ltd., UK for his research.

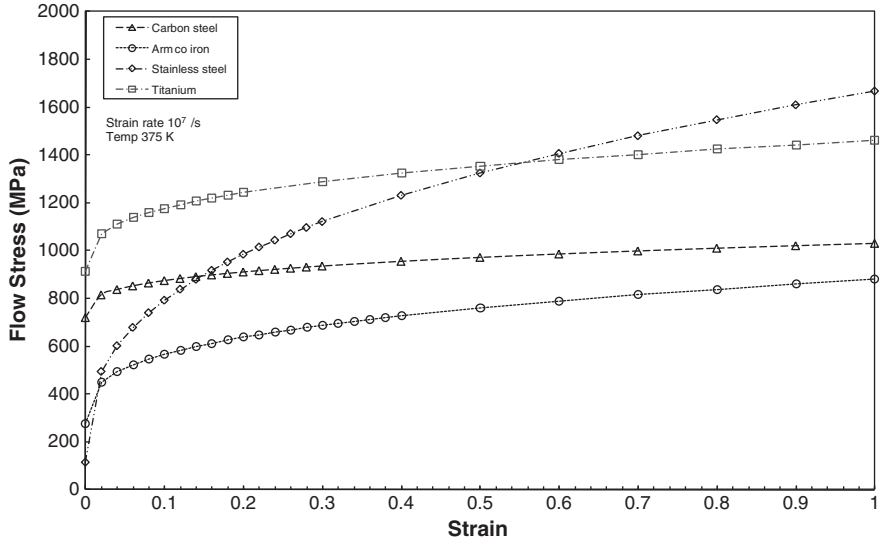

Fig. 4. Flow stress of titanium, carbon steel, Armco iron and austenitic stainless steel as a function of strain at strain rate 10^7/s and 375 K according to the J–C model with data from Table 3.

References

[1] H. Assadi, F. Gartner, T. Stoltenhoff, H. Kreye, Acta Mater. 51 (2003) 4379.
[2] T. Schmidt, F. Gaertner, H. Kreye, J. Therm. Spray Technol. 15 (2006) 488.
[3] T. Schmidt, F. Gartner, H. Assadi, H. Kreye, Acta Mater. 54 (2006) 729.
[4] T. Marrocco, D.G. McCartney, P.H. Shipway, A.J. Sturgeon, J. Therm. Spray Technol. 15 (2006) 263.
[5] C.-J. Li, W.-Y. Li, Surf. Coat. Technol. 167 (2003) 278.
[6] W.Y. Li, C. Zhang, X.P. Guo, J.L. Xu, C.J. Li, H.L. Liao, C. Cocidet, K.A. Khor, Adv. Eng. Mater. 9 (2007) 418.
[7] H.-R. Wang, B.-R. Hou, J. Wang, Q. Wang, W.-Y. Li, J. Therm. Spray Technol. 17 (2008) 736.
[8] S.H. Zahiri, D. Fraser, M. Jahedi, J. Therm. Spray Technol. 18 (2009) 16.
[9] S.H. Zahiri, S.C. Mayo, M. Jahedi, Microsc. Microanal. 14 (2008) 260.
[10] S.H. Zahiri, W. Yang, M. Jahedi, J. Therm. Spray Technol. 18 (2009) 110.
[11] T. Hussain, D. McCartney, P. Shipway, T. Marrocco, J. Therm. Spray Technol. 20 (2010) 260.
[12] M. Ghosh, S. Chatterjee, Mater. Charact. 48 (2002) 393.
[13] G.B. Kale, R.V. Patil, P.S. Gawade, J. Nucl. Mater. 257 (1998) 44.
[14] T.H. Van Steenkiste, J.R. Smith, R.E. Teets, Surf. Coat. Technol. 154 (2002) 237.
[15] M. Grujicic, J.R. Saylor, D.E. Beasley, W.S. DeRosset, D. Helfritch, Appl. Surf. Sci. 219 (2003) 211.
[16] T. Stoltenhoff, H. Kreye, H.J. Richter, J. Therm. Spray Technol. 11 (2002) 542.
[17] C.J. Li, W.Y. Li, H.L. Liao, J. Therm. Spray Technol. 15 (2006) 212.
[18] C.J. Li, H.T. Wang, Q. Zhang, G.J. Yang, W.Y. Li, H. Liao, J. Therm. Spray Technol. 19 (1–2) (2010) 95.
[19] T. Schmidt, H. Assadi, F. Gärtner, H. Richter, T. Stoltenhoff, H. Kreye, T. Klassen, J. Therm. Spray Technol. 18 (2009) 794.
[20] G. Bae, Y. Xiong, S. Kumar, K. Kang, C. Lee, Acta Mater. 56 (2008) 4858.
[21] D. Zhang, P.H. Shipway, D.G. McCartney, J. Therm. Spray Technol. 14 (2005) 109.
[22] P. King, G. Bae, S. Zahiri, M. Jahedi, C. Lee, J. Therm. Spray Technol. 19 (2010) 620.
[23] P.C. King, S.H. Zahiri, M. Jahedi, Acta Mater. 56 (2008) 5617.
[24] G. Bae, K. Kang, J.-J. Kim, C. Lee, Materials Science and Engineering: A, 527 (2010) 6313–6319.
[25] G. Bae, K. Kang, H. Na, C. Lee, in: B.R. Marple, M.M. Hyland, Y.-C. Lau, C.-J. Li, R.S. Lima, G. Montavon (Eds.), Thermal Spray 2009: Expanding Thermal Spray Performance to New Markets and Applications, ASM International, Las Vegas, NV, 2009, p. 290.
[26] G. Bae, S. Kumar, S. Yoon, K. Kang, H. Na, H.-J. Kim, C. Lee, Acta Mater. 57 (2009) 5654.
[27] R.R. Chromik, D. Goldbaum, J.M. Shockley, S. Yue, E. Irissou, J.-G. Legoux, N.X. Randall, Surf. Coat. Technol. 205 (2010) 1409–1414.
[28] S. Gulizia, B. Tiganis, M.Z. Jahedi, N. Wright, T. Gengenbach, C. MacRae, in: B.R. Marple, M.M. Hyland, Y.-C. Lau, C.-J. Li, R.S. Lima, G. Montavon (Eds.), Thermal Spray 2009: Expanding Thermal Spray Performance to New Markets and Applications, ASM International, Las Vegas, NV, 2009, p. 237.
[29] C.K.S. Moy, J. Cairney, G. Ranzi, M. Jahedi, S.P. Ringer, Surf. Coat. Technol. 204 (2010) 3739.
[30] D. Rafaja, T. Schucknecht, V. Klemm, A. Paul, H. Berek, Surf. Coat. Technol. 203 (2009) 3206.
[31] W. Wong, A. Rezaeian, E. Irissou, J.-G. Legoux, S. Yue, Adv. Mater. Res. 89–91 (2010) 639.
[32] S.H. Zahiri, C.L. Antonio, M. Jahedi, J. Mater. Process. Technol. 209 (2009) 922.
[33] S.H. Zahiri, M. Jahedi, W. Yang, in: E. Lugscheider (Ed.), Thermal Spray: Global Coating Solutions, ASM International, Maastricht, The Netherlands, 2008.
[34] E. Calla, Mechanical, Material and Manufacturing Engineering, University of Nottingham, 2005.
[35] W. Wong, E. Irissou, A. Ryabinin, J.-G. Legoux, S. Yue, J. Therm. Spray Technol. 20 (2011) 213.
[36] K. Binder, J. Gottschalk, M. Kollenda, F. Gärtner, T. Klassen, J. Therm. Spray Technol. 20 (2011) 234.
[37] D. Christoulis, S. Guetta, V. Guipont, M. Jeandin, J. Therm. Spray Technol. 20 (2011) 523.
[38] J.W. Wu, H.Y. Fang, S. Yoon, H. Kim, C. Lee, Scr. Mater. 54 (2006) 665.
[39] M. Itabashi, K. Kawata, Intl. J. Impact Eng. 24 (2000) 117.
[40] T. Hussain, A Study of Bonding Mechanisms and Corrosion Behaviour of Cold Sprayed Coatings, University of Nottingham, 2011.
[41] G.R. Johnson, W.H. Cook, Eng. Fract. Mech. 21 (1985) 31.
[42] K. Yokoyama, M. Watanabe, S. Kuroda, Y. Gotoh, T. Schmidt, F. Gartner, Mater. Trans. 47 (2006) 1697.
[43] I.M. Hutchings, J. Phys. D Appl. Phys. 10 (1977) L179.
[44] M.C. Shaw, Metal Cutting Principles, Clarendon, , 1984.
[45] Y. Yang, Z. Xinming, L. Zhenghua, L. Qingyun, Acta Mater. 44 (1996) 561.
[46] Y. Yang, B.F. Wang, J. Mater. Sci. 41 (2006) 7387.